Using a Depth Heuristic for Light Field Volume Rendering

Seán Martin[1], Seán Bruton[1], David Ganter[1] and Michael Manzke[1]
[1]*School of Computer Science and Statistics, Trinity College Dublin, College Green, Dublin 2, Ireland*
{*martins7, sbruton, ganterd*}*@tcd.ie, michael.manzke@cs.tcd.ie*

Keywords: Light Fields, View Synthesis, Convolutional Neural Networks, Volume Rendering, Depth Estimation, Image Warping, Angular Resolution Enhancement.

Abstract: Existing approaches to light field view synthesis assume a unique depth in the scene. This assumption does not hold for an alpha-blended volume rendering. We propose to use a depth heuristic to overcome this limitation and synthesise views from one volume rendered sample view, which we demonstrate for an 8×8 grid. Our approach is comprised of a number of stages. Firstly, during direct volume rendering of the sample view, a depth heuristic is applied to estimate a per-pixel depth map. Secondly, this depth map is converted to a disparity map using the known virtual camera parameters. Then, image warping is performed using this disparity map to shift information from the reference view to novel views. Finally, these warped images are passed into a Convolutional Neural Network to improve visual consistency of the synthesised views. We evaluate multiple existing Convolutional Neural Network architectures for this purpose. Our application of depth heuristics is a novel contribution to light field volume rendering, leading to high quality view synthesis which is further improved by a Convolutional Neural Network.

1 INTRODUCTION

Light field technology is an exciting emergent subject, allowing for extremely rich capture and display of visual information. Generating a light field from volumetric data produces significant perceptual enhancements over directly volume rendering an image. For example, medical practitioners could view the result of Magnetic Resonance Imaging (MRI) scans in real-time using a near-eye light field virtual reality device (Lanman and Luebke, 2013) or The Looking Glass (Frayne, 2018) without the drawback of current display devices, such as a single focal plane. These visualisations would allow for deeper understanding of a patient's anatomy before surgery and open new avenues for medical training. Although direct volume rendering is possible in real-time for a single viewpoint, this is infeasible with current technology for a full light field due to the necessary increase in pixel count. To bring the performance closer to interactive rates, we propose a view synthesis method for light field volume rendering by inferring pixel values using a single sample image.

Recently, Convolutional Neural Networks (CNNs) have been applied to view synthesis for light fields of natural images, with the deep learning approaches of (Wu et al., 2017) and (Kalantari et al., 2016) constituting state of the art. (Srinivasan et al., 2017) showed notable results using only one image from a camera to synthesise an entire light field. However, these methods are designed for natural images which can reasonably be assumed to have a well-defined depth. This is not the case for volume rendering due to alpha compositing not always resulting in an opaque surface. To increase the suitability of these methods for volume rendering, we present novel modifications.

Our proposed method synthesises a light field from a single volume rendered sample image, which we demonstrate for an 8×8 angular resolution light field. We represent the light field as a structured grid of images captured by a camera moving on a plane, with the number of images referred to as the angular resolution. A depth heuristic is used to estimate a depth map during volume ray casting, inspired by the work of (Zellmann et al., 2012). This depth map is converted to a disparity map using the known virtual camera parameters. Image warping is performed using the disparity map to shift information from the single reference view to all novel view locations. Finally, the disparity map and warped images are passed into a CNN to improve the visual consistency of the synthesised views.

The results of this research show that the depth heuristic applied during volume rendering produces high quality image warping. Moreover, the CNN increases the visual consistency of synthesised views, especially for those views at a large distance from the sample reference view, but the CNN must be retrained for new volumes and transfer functions. Although the presented method is not faster than directly volume rendering a light field, it is fast compared to existing light field angular resolution enhancement approaches. The bottleneck is the image warping procedure, which takes 90% of the total time to synthesise a light field, as opposed to our depth heuristic calculation or CNN. Our method is beneficial for complex volumes because the time to synthesise a light field is independent of the size and complexity of the volume and rendering techniques.

2 RELATED WORK

Light Field View Synthesis There are two primary paradigms for synthesising views for light fields of natural images. One paradigm is to estimate some form of geometry in the scene, commonly depth, and base the view synthesis on this geometry. The other paradigm focuses on the structure of light fields, using expected properties of Epipolar-Plane Images (EPIs) for view synthesis (Wu et al., 2017), or transforming the problem to other domains with well-defined behaviour (Shi et al., 2014; Vagharshakyan et al., 2018). These structure based approaches are slower than directly rendering the light field and are not applicable to this problem. For instance, testing the state of the art method by (Wu et al., 2017) was prohibitively slow, taking 16 minutes to synthesise a full light field.

(Yoon et al., 2015) interpolated sets of light field sub-aperture images with CNNs to produce a $\times 2$ angular resolution enhancement. This approach does not take advantage of the light field structure and the resulting resolution enhancement is too low to be useful for volume rendering. Using a soft three dimensional (3D) reconstruction (Penner and Zhang, 2017) produces high quality view synthesis, but as we have a 3D volume available, this route is not useful for us. (Wanner and Goldluecke, 2014) formulate the view synthesis problem as a continuous inverse problem, but optimising the associated energy is too slow for our needs.

Depth-based approaches are particularly relevant to our problem, since we can estimate depth using volumetric information. One such approach by (Kalantari et al., 2016) uses deep learning to estimate depth and colour, but they synthesise the light field view by view. This leads to slow performance, taking roughly 12.3 seconds to generate a single novel view from four input images of 541×376 resolution.

(Srinivasan et al., 2017) tackled the problem of synthesising a four dimensional (4D) light field from a single image. This problem is ill-posed because a single image of a light field contains inadequate information to reconstruct the full light field. The authors alleviate this by using data-driven techniques trained on images of objects from specific categories (e.g. flowers) and by taking advantage of redundancies in the light field structure. Their method accounts for specular highlights, rather than assuming that all surfaces exhibit diffuse reflection. This is very relevant for volume rendering, as surfaces are often anisotropically shaded. In contrast to most approaches, they produce all novel views at once instead of synthesising each view separately. This is fast, synthesising a $187 \times 270 \times 8 \times 8$ light field in under one second on a NVIDIA Titan X Graphics Processing Unit (GPU). Because of the speed of this approach, the single input view required, and the high quality results, our approach follows a similar formulation.

To make the method of (Srinivasan et al., 2017) more suitable for volume rendering, we propose to use a depth heuristic during volume rendering as opposed to estimating depth for each ray in the light field with a CNN. This will increase speed and account for the transparent surfaces in volume rendering. Additionally, we propose to apply a two dimensional (2D) CNN to improve the quality of the novel views instead of their slower and potentially unnecessary 3D CNN.

CNN Architectures for 4D Light Fields Although we have volumetric information available, CNNs using images from multiple views usually perform better than 3D CNNs on volumetric data because current deep learning architectures are often unable to fully exploit the power of 3D representations (Qi et al., 2016). Due to limitations of 3D CNNs, (Wang et al., 2016) demonstrate how to map a 4D light field into a 2D VGG network (Simonyan and Zisserman, 2014) instead of using a 3D CNN. This is beneficial as the weights of a pre-trained 2D model can be updated. Additionally, although the 4D filters in 3D CNNs are intuitive to use on a 4D light field, the number of parameters quickly explode. Since their paper is aimed towards material recognition, we experiment with the two most relevant methods for view synthesis to map a 4D light field into a 2D CNN.

View Synthesis for Volume Rendering Accelerating volume rendering has long been an active research area. Warping information from sample views to synthesise new views (Mark et al., 1997; Mueller et al., 1999; Lochmann et al., 2016) is feasible be-

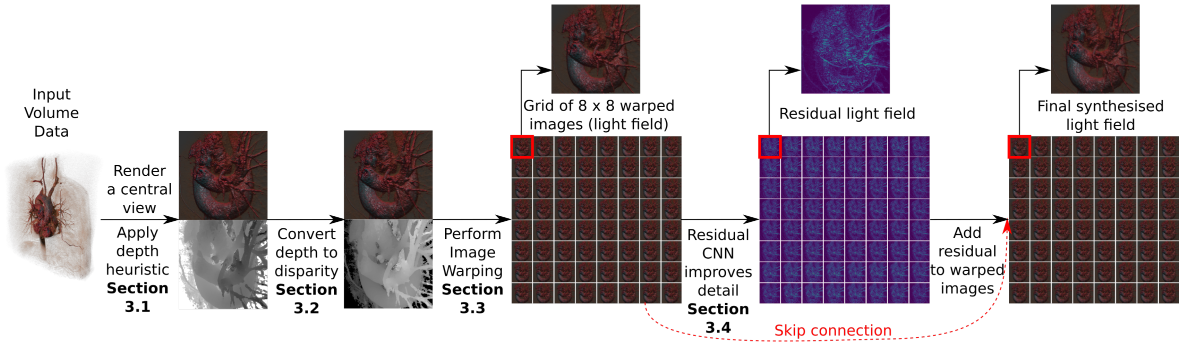

Figure 1: Our proposed light field synthesis method can be broken down into distinct stages, including an initial depth heuristic calculation stage and a final CNN stage acting as a residual function to improve fine-grained detail.

cause rendered images do not tend to change dramatically between viewpoints. Warping images is particularly prevalent in remote rendering because a remote machine with no GPU can warp an image produced by a server until a new image is received. (Zellmann et al., 2012) proposed to warp images received from a remote server based on an additional depth channel. Due to alpha compositing resulting in transparent surfaces with ill-defined depths, the authors present multiple depth heuristics for image warping. They found that modifying the ray tracer to return depth at the voxel where the accumulated opacity along the ray reaches 80% was the best balance between speed and accuracy. We propose to apply an improved depth heuristic to light field view synthesis for volume rendering.

3 METHODOLOGY

Our goal is to synthesise a volume rendered light field as a structured set of 8×8 novel views. The following steps are involved in our light field synthesis (Figure 1).

1. Render a reference view by direct volume rendering and use a depth heuristic to estimate a depth map during ray casting.
2. Convert the depth map to a disparity map using the camera parameters.
3. Applying backward image warping to the reference view using the disparity map to approximate a light field with an 8×8 angular resolution.
4. Apply a CNN to the warped images to improve visual consistency. This is modelled as a residual function which is added to the approximate light field from the previous step.

We apply a CNN to help account for inaccuracies in the depth map, specular highlights, and occlusions to improve the visual coherency of synthesised views over depth-based image warping.

3.1 Volume Depth Heuristics

Part of our contribution is applying depth heuristics in volume rendering for light field angular resolution enhancement. Depth maps are useful for image warping, but there is no unique depth for an alpha-blended volume, so we apply a heuristic to determine a per-pixel depth map. The depth of the first non-transparent voxel along the ray is inaccurate as it tends to be corrupted by highly transparent volume information close to the camera. Using isosurfaces gives a good view of depth, but these must be recalculated during runtime if the volume changes. To produce a more accurate depth map, we estimate a depth during ray casting.

To produce a depth estimate, we improve upon the best performing single pass depth heuristic from (Zellmann et al., 2012). In their work, when a ray accumulates a fixed amount of opacity, the depth of the current voxel is saved. However, this depth map is often missing information when a ray does not accumulate the desired opacity. To counteract this limitation, we save a depth value when a ray accumulates a low threshold opacity and overwrite that depth if the ray later accumulates the high threshold opacity. This improved the quality of the depth map and a comparison of different depth heuristics is presented in Section 5.2.

3.2 Converting Depth to Disparity

We convert depth to disparity for image warping. During rendering, a depth value from the Z-buffer $Z_b \in [0,1]$ is converted to a pixel disparity value using the intrinsic camera parameters as follows. The depth buffer value Z_b is converted into normalised device co-ordinates, in the range $[-1,1]$, as $Z_c = 2 \cdot Z_b - 1$.

Then, perspective projection is inverted to give depth in eye space as

$$Z_e = \frac{2 \cdot Z_n \cdot Z_f}{Z_n + Z_f - Z_c \cdot (Z_f - Z_n)} \quad (1)$$

Where Z_n and Z_f are the depths of the camera's near and far clipping planes in eye space, respectively. Note that Z_n should be set as close to the visualised object as possible to improve depth buffer accuracy, while Z_f has negligible effect on the accuracy. Given eye depth Z_e, it is converted to a disparity value d_r in real units using similar triangles (Wanner et al., 2013) as

$$d_r = \frac{B \cdot f}{Z_e} - \Delta x \quad (2)$$

Where B is the camera baseline, or distance between two neighbouring cameras in the grid, f is the focal length of the camera, and Δx is the distance between two neighbouring cameras' principle points. Again, using similar triangles, the disparity in real units is converted to a disparity in pixels as

$$d_p = \frac{d_r W_p}{W_r} \quad (3)$$

Where d_p and d_r denote the disparity in pixels and real world units respectively, W_p is the image width in pixels, and W_r is the image sensor width in real units. If the image sensor width in real units is unknown, W_r can be computed from the camera field of view θ and focal length f as $W_r = 2 \cdot f \cdot \tan(\frac{\theta}{2})$.

3.3 Disparity Based Image Warping

Using the volume rendered reference view and estimated disparity map, we warp the reference view to 63 novel positions in a grid. To synthesise a novel view, a disparity map $D : \mathbb{R}^2 \mapsto \mathbb{R}$ is used to relate pixel locations in a novel view to those in the reference view. Let $I : \mathbb{R}^2 \mapsto \mathbb{R}^3$ denote a reference Red Green Blue (RGB) colour image at grid position $(u_r,\ v_r)$ with an associated pixel valued disparity map D. Then a synthesised novel view I' at grid position $(u_n,\ v_n)$ can be formulated as:

$$I'(x + d \cdot (u_r - u_n),\ y + d \cdot (v_r - v_n)) = I(x,\ y) \quad \text{where} \quad d = D(x,\ y) \quad (4)$$

There are two paradigms for image warping with a disparity map; forward mapping and backward mapping. Forward mapping is not surjective and maps pixels from the reference view into the novel view, which results in holes in the image, for example, in occluded areas. Backward mapping works in the inverse direction. For each pixel in the novel view, the most relevant information from the reference view is assigned to that pixel. Therefore, it is surjective and no holes are formed, but the reference view is usually oversampled. A comparison between backwards mapping and forward mapping in terms of Peak Signal to Noise Ratio (PSNR) and Structural Similarity (SSIM) is presented in Figure 2.

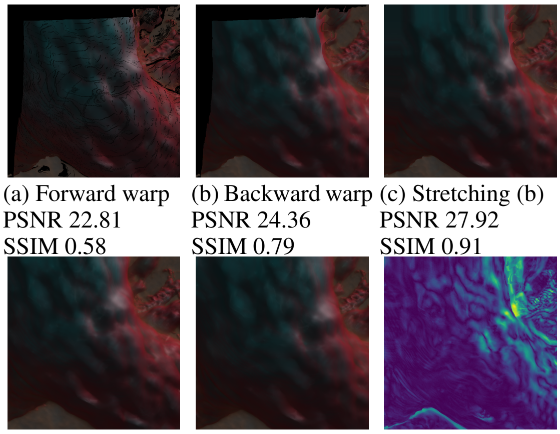

(a) Forward warp PSNR 22.81 SSIM 0.58
(b) Backward warp PSNR 24.36 SSIM 0.79
(c) Stretching (b) PSNR 27.92 SSIM 0.91
(d) Central reference
(e) Ground truth image
(f) Difference between (c) and (e)

Figure 2: Demonstrating different warping methods to synthesise the top left novel view at grid position $(0,0)$ from the central reference view at position $(4,4)$ shown in Figure (d). The forward warping in (a) has many cracks and holes. Backward warping in (b) is smooth but is missing information at the borders. As such, the border is stretched in (c), which represents the final backward warping used.

For backward warping, pixels in the novel view that should read data from a location that falls outside the border of the reference view were set to read the closest border pixel in the reference view instead. This would stretch the border of the reference view in the novel view, rather than produce holes (Figure 2(c)).

3.4 Convolutional Neural Network

We apply a CNN to the grid of 64 images from the previous step to improve the visual quality of the synthesised light field. Giving the CNN access to all warped images and the estimated disparity map allows the network to learn to correct for errors at object borders, modify the effect of specular highlights, and predict information which is occluded in the reference view. This is achieved by framing the network as a residual function that predicts only the corrections needed to be made to the warped images to reduce the synthesis loss. The residual light field has full range over the colour information, with values in $[-1, 1]$, to allow for removal of erroneous pixels and addition of predicted data.

Because the light field is 4D, 3D CNNs which use

4D filters are intuitive to apply to this problem, but using 2D convolutions leads to faster performance. (Wang et al., 2016) demonstrated strong evidence that 3D CNNs can be effectively mapped into 2D architectures. To experiment with this, four primary network architectures were implemented. Note that any network's Rectified Linear Unit activations have been replaced by Exponential Linear Unit activations to be consistent with the network from (Srinivasan et al., 2017).

The first network tested was the 3D occlusion prediction network from (Srinivasan et al., 2017), which we will label **Srinivasan3D**. This network is structured as a residual network with $3 \times 3 \times 3$ filters that have access to every view. The input to Srinivasan3D is all 64 warped images, and a colour mapped disparity map.

(He et al., 2016) introduced the concept of residual networks, which perform a series of residual functions. The second network tested was a modified version of ResNet18 (He et al., 2016), which we will call **StackedResNet**. The input to StackedResNet is all warped images and a colour mapped disparity map which are stacked over the colour channels, a 195 channel input. To keep the spatial input dimensions fixed, all spatial pooling is removed from ResNet18. The first layer of ResNet18 is also replaced, as it is intended to gather spatial information, and the input is instead convolved into 64 features to gather angular information. The final fully connected layer of ResNet18 is replaced by a convolutional layer with a tanh activation function. Due to the removal of pooling, pre-trained weights were not used for StackedResNet.

The third network, labelled **StackedEDSR**, was based on the Enhanced Deep Super-Resolution (EDSR) network of (Lim et al., 2017). EDSR is modelled as a series of residual blocks which act upon a single RGB image to learn relevant features before performing spatial upsampling. The input to StackedEDSR is the same as StackedResNet. As such, we modify the first convolutional layer of EDSR to map 195 colour channels, instead of 3 colour channels, to 256 features. StackedEDSR also removes the final spatial upscaling performed by EDSR and applies tanh activation after the last layer.

The final network, denoted **AngularEDSR**, is the same network as EDSR, except for removal of spatial upscaling at the last layer and application of tanh activation at the final layer. To map the input into the three colour channel input required for EDSR, angular remapping from (Wang et al., 2016) is applied to create an RGB colour image. Consider a light field sample with 8×8 images having 512×512 pixels and three colour channels. This would be remapped into an image having $(8 \cdot 512) \times (8 \cdot 512)$ pixels and three colour channels. In this remapped image, the uppermost 8×8 pixels would contain the upper-left pixel from each of the original 8×8 views. The 3×3 filters used in this architecture look at the nearest neighbours to a view as opposed to all views as is the case for the other networks tested. Pre-trained weights were tested for both EDSR based networks, but they performed poorly.

4 IMPLEMENTATION

Every experiment was performed on a computer with 16GB memory, an Intel i7-7700K @ 4.20GHz Central Processing Unit (CPU), and a NVIDIA GeForce GTX 1080 GPU running on Ubuntu 16.04. For deep learning, the PyTorch library (Paszke et al., 2017), version 0.40 was used with Cuda 9.1, cuDNN 7.1.2, and NVIDIA driver version 390.30.

4.1 Data Collection

To demonstrate validity of the proposed method, an MRI of a heart with visible aorta and arteries would be used for training and validation. The heart volume dataset has a resolution of $512 \times 512 \times 96$ and is available online (Roettger, 2018b). See Figure 3 for examples of this dataset rendered. This volume was chosen because the heart has a rough surface, and the aorta and arteries create intricate structures which are difficult to reconstruct. See Figure 3(c) for an example of a translucent structure in this dataset. The applied transfer function does not contain high frequencies which tend to reveal isosurfaces or geometry which is static in texture because inaccurate depth maps can still produce correct warping on large regions with a static texture. Consequently, the depth map generation is well tested.

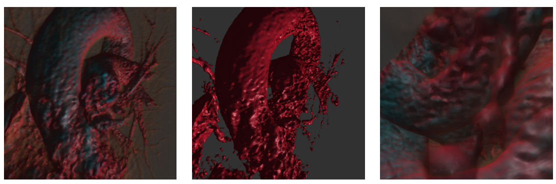

(a) Training transfer function (b) Simple transfer function (c) Translucent structure

Figure 3: Demonstrating the training volume and transfer function with images rendered in Inviwo.

Using Inviwo (Sundén et al., 2015), a synthetic light field dataset is captured. The light field capturing geometry used is a "2D array of outward look-

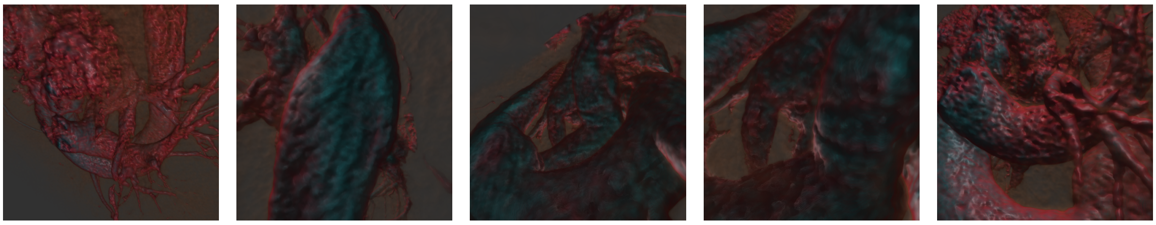

Figure 4: Sample training light field central sub-aperture views.

ing (non-sheared) perspective views with fixed field of view" (Levoy and Hanrahan, 1996). To capture the synthetic dataset, a Python script is created to move the camera in Inviwo along a regular equidistant grid. The cameras are shifted along the grid rather than rotated to keep their optical axes parallel, removing the need to rectify the images to a common plane. Each light field sample has an angular resolution of 8×8, with 512×512 spatial resolution. 2000 training light fields are captured, and 100 separate validation light fields. See Figure 4 for the central sub-aperture image of five captured light fields.

Sampling was performed uniformly, rather than focusing on particular sections of the heart. To increase the diversity of the data captured, a plane with a normal aligned with the camera view direction is used to clip the volume for half the captured examples. This plane clipping can reveal detailed structures inside the volume and demonstrates the accuracy of the depth heuristic when the volume changes.

4.2 Training Procedure

To increase training speeds and the amount of available data, four random spatial patches of size 128×128 are extracted from each light field at every training epoch. Additionally, training colour images have a random gamma applied as data augmentation.

The CNNs are trained by minimising the per-pixel mean squared error between the ground truth views and the synthesised views. Network optimisation was performed with Stochastic gradient descent and Nesterov momentum. An initial learning rate of 0.1 was updated during learning by cosine annealing the learning rate with warm restarts (Loshchilov and Hutter, 2017). Gradients were clipped based on the norm at a value of 0.4 and an L2 regularisation factor of 0.0001 was applied. Training takes about 14 hours using 2D CNN architectures with eight CPU cores used for data loading and image warping.

5 EXPERIMENTS

5.1 Network Comparison for View Synthesis

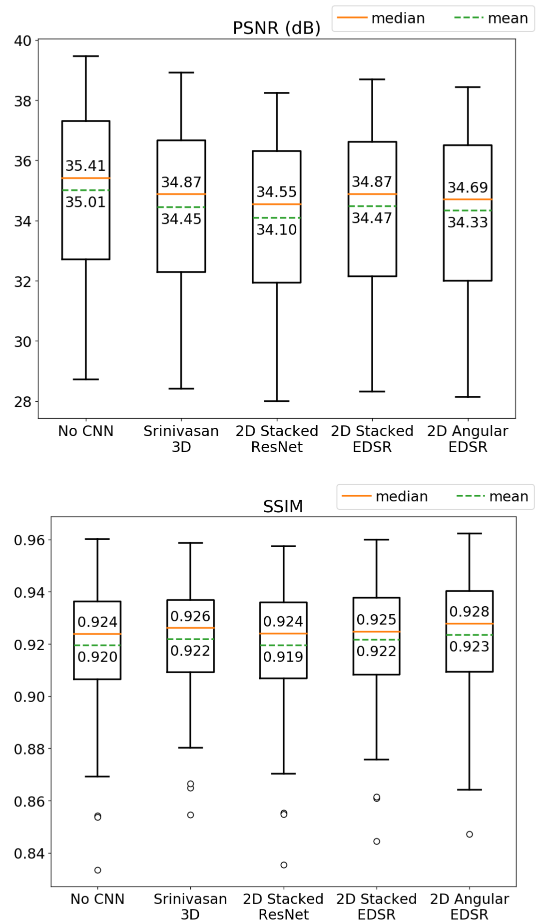

Figure 5: Comparing CNN architectures for view synthesis. The box plots show PSNR and SSIM values averaged over the 64 grid images for one hundred validation light fields. The whiskers in the box plot indicate the data variability and show the lowest datum and highest datum within 1.5 of the interquartile range. The small circlular points outside of the whiskers are outliers. The CNNs incur large loss at the reference view position, especially for PSNR.

In Figure 5, the PSNR and SSIM metrics for each network averaged over all light field sub-aperture images are presented for the full validation set of one hundred light fields. These experiments demonstrate that the 3D convolutions performed in (Srinivasan et al., 2017) can be effectively mapped into 2D CNNs as the EDSR (Lim et al., 2017) based 2D networks outperform the slower 3D convolutions.

From Figure 5, it appears that none of the residual CNNs exhibit much performance difference from geometrical warping. Investigating the results for each synthesised sub-aperture view reveals further insights. This is emphasised by the large loss in PSNR and SSIM for the reference view position when using a CNN. Warping does not change the reference view, maintaining perfect PSNR of 100 and SSIM of 1.0. However, when a residual CNN is applied it modifies the reference view and this decreases to approximately 40 and 0.92 respectively. The reference view could be used without adding the residual to it, but this lessens the consistency of the resulting light field.

Figure 6 presents the difference in quality between image warping and the AngularEDSR CNN per sub-aperture image location for one sample validation light field. To summarise the results, images far away from the central view exhibited lower loss when a residual CNN was applied on top of image warping. However, the CNN caused a degradation in quality for central images. Additional evaluation performed with the Learned Perceptual Image Patch Similarity (LPIPS) metric (Zhang et al., 2018) using the deep features of AlexNet (Krizhevsky et al., 2012) to form a perceptual loss function agrees with the per image values for SSIM and PSNR. See Figure 8 for the bottom right sub-aperture view of this light field from the validation set along with difference images to visualise the effect of the CNN.

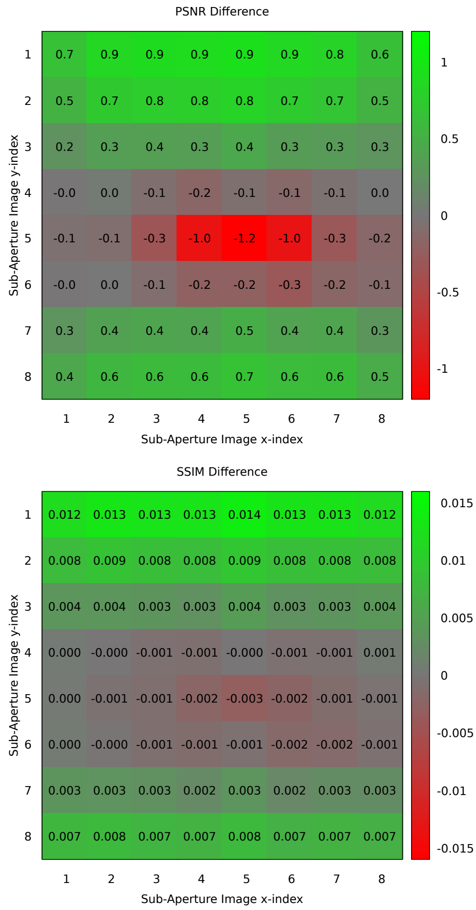

Figure 6: SSIM and PSNR difference after applying AngularEDSR to the warped images. Results are shown per sub-aperture image location in an 8×8 grid. Position $(5,5)$ is the location of the reference view and the loss in PSNR at that position is scaled to make the graph more readable.

5.2 Depth Heuristic Comparison

To compare depth heuristics, ten light fields were captured without volume clipping. Five depth maps are recorded:

1. **OneDepth**: The depth at 0.8 opacity during ray casting.
2. **TwoDepthFar**: The depth at 0.8 opacity, and if that is not reached, the depth at 0.3 opacity during ray casting.
3. **TwoDepthClose**: The depth at 0.7 opacity, and if that is not reached, the depth at 0.35 opacity during ray casting.
4. **IsoDepth**: The depth of an isosurface at a value of 80 which is precomputed on the CPU.
5. **FirstDepth**: The depth of the first non-transparent voxel hit during ray casting.

Each of these depth maps is used to warp the central light field sample image to all 64 grid locations. The average PSNR and SSIM over the ten synthesised light fields for each different depth map is presented in Table 1. TwoDepthFar is the depth heuristic that was selected for use in the training set, as it achieved the highest SSIM in this experiment.

Table 1: Comparing quantitative results of image warping with different depth maps averaged over 10 light fields.

Depth map type	PSNR	SSIM
OneDepth	34.63	0.907
TwoDepthFar	35.95	**0.923**
TwoDepthClose	**35.97**	0.922
IsoDepth	35.01	0.909
FirstDepth	27.96	0.802

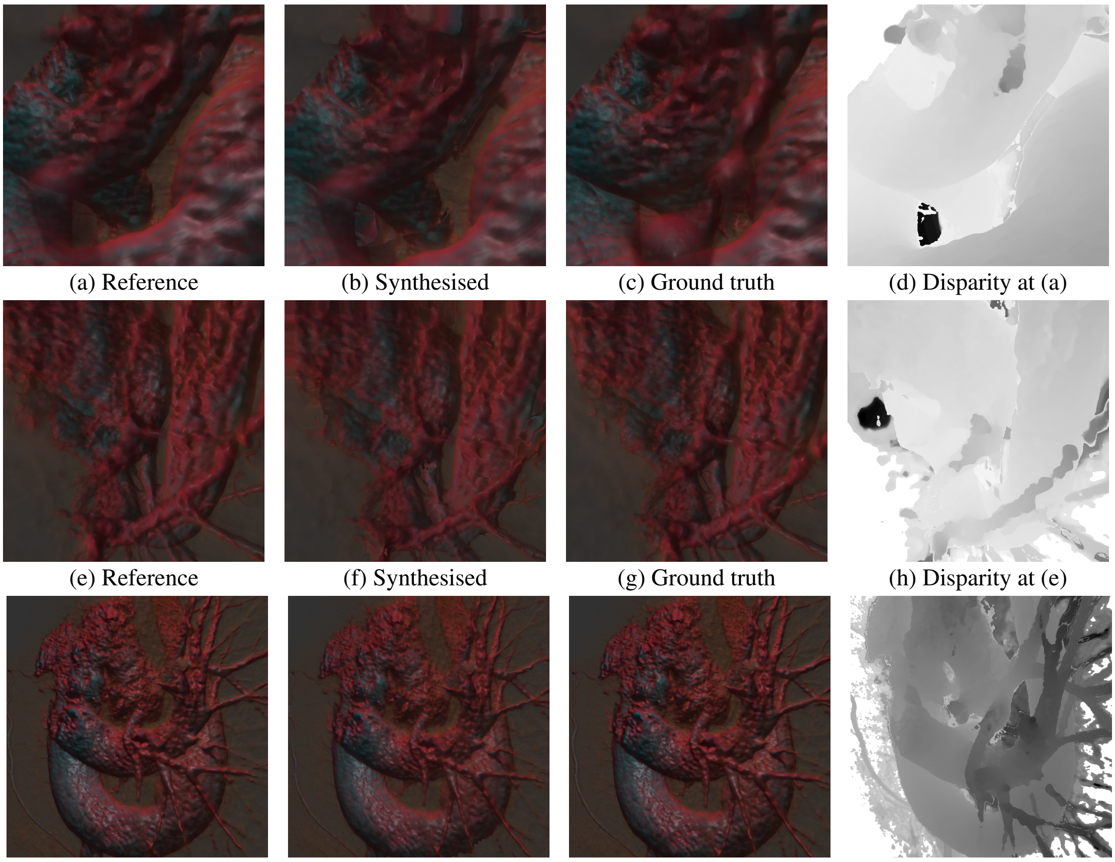

(a) Reference (b) Synthesised (c) Ground truth (d) Disparity at (a)

(e) Reference (f) Synthesised (g) Ground truth (h) Disparity at (e)

(i) Reference (j) Synthesised (k) Ground truth (l) Disparity at (i)

Figure 7: Example synthesised upper-left images from the validation set. The first row has low performance due to the translucent structure at the centre of the view. The second row has middling performance since the arteries are not perfectly distinguished from the aorta. The third row has high performance with small inaccuracies, such as on the lower right edge of the aorta. Disparity maps for the central reference views are presented in the final column.

5.3 Example Synthesised Light Fields

To investigate the method performance, an example of a low, middling, and high quality synthesised light field from the validation set is presented in Figure 7. Figure 7(b) is a poor reconstruction due to the opaque structure that should be present in the centre of the view. This structure is not picked up by the disparity map, resulting in a large crack appearing in the synthesised image. Figure 7(f) is a reasonably well synthesised view. Most of the information is accurately shifted from the reference view, but some arteries lose their desired thickness and the image is not very sharp. Figure 7(j) is an accurate synthesis. Some errors are seen around object borders, such as on the arch of the aorta, but overall it is hard to distinguish from the ground truth information. Additional results are presented in a supplementary video.

5.4 Time Performance in Inviwo

The presented method is currently not fast enough for light field volume rendering at interactive rates. On average, synthesising and displaying a light field of 64 images with 512×512 pixels from the heart MRI discussed in Section 4.1 takes 3.73 seconds in Inviwo (Sundén et al., 2015) if bilinear interpolation is used for backward warping with the AngularEDSR network. If nearest neighbours is used for warping instead of bilinear interpolation the whole process takes 1.28 seconds, disregarding the time to pass information through Inviwo. This is similar to the time taken to directly render a light field in Inviwo, which takes 1.18 seconds.

The time for CNN view synthesis has far less deviation than directly volume rendering a light field, because the latter depends heavily on the complexity of the scene. A CNN performs the same operations regardless of input complexity, which results in steady performance. Additionally, the CNN per-

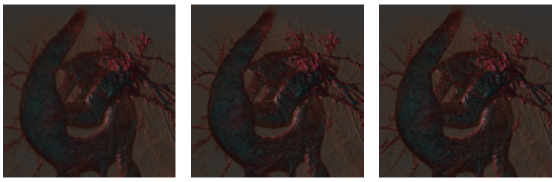

(a) AngularEDSR PSNR 36.05 SSIM 0.909 (b) Warping alone PSNR 35.59 SSIM 0.903 (c) Ground truth PSNR 100.0 SSIM 1.000

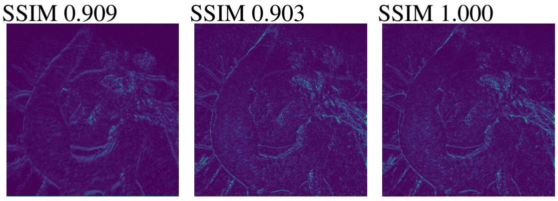

(d) Difference of (a) and (b) (e) Difference of (a) and (c) (f) Difference of (b) and (c)

Figure 8: The bottom right view in the light field which Figure 6 presents results for. Figure (d) visualises the residual applied by the CNN to the warped images to improve visual quality. The CNN detects broad edges to improve, such as the central arch of the aorta, but fails to improve finer details such as the arteries in the top right of the image.

formance is agnostic to the resolution of the volume data and only depends on the spatial resolution of the reference image. Accordingly, for very large complex volumes with expensive rendering techniques, this method could be applicable.

To understand the bottlenecks, we analyse the breakdown of the 3.73 seconds to synthesise and display a light field in Inviwo with bilinear interpolation. Rendering the reference view and passing input and output information through Inviwo takes 0.91 seconds on average. Only 0.003 seconds is spent on applying the depth heuristic, which is implemented in the fragment shader. All CNNs tested complete a forward pass in less than 0.2 seconds, with AngularEDSR taking 0.047 seconds and Srinivasan3D taking 0.19 seconds. The time performance bottleneck is image warping, which takes approximately 2.77 seconds to warp a 512×512 image to a grid of 8×8 locations on the CPU. This is performed with bilinear interpolation of pixel values. Using nearest neighbours does not significantly jeopardise quality, and takes 1.17 seconds. Although our image warping is performed on the CPU due to GPU memory limitations, the GPU based warping from (Srinivasan et al., 2017) is also a performance bottleneck. For images of size 192×192, their GPU accelerated warping takes 0.13 seconds, while our CPU warping with bilinear interpolation takes 0.17 seconds.

Because of the time drawback, a 3D CNN which directly took a reference view and associated depth map to perform view synthesis was tested. This took only 0.49 seconds on average, which is faster than direct volume rendering. Despite this, the results were low quality, averaging 26.1 PSNR and 0.83 SSIM. The CNN learnt how to move information to new views, but the colour consistency between views was low. This method could be improved by a loss which penalises a lack of colour consistency between views.

5.5 Performance on Unseen Data

Although the depth heuristic used during volume rendering seems reasonable, there is no guarantee it would perform well with different volumes and transfer functions (TFs). Three experiments were performed with the AngularEDSR architecture on ten sample light fields in each case to test generalisation of the depth heuristic. A new volume set of a head MRI was used, available online (Roettger, 2018a) with a different TF from the training set. Results are presented in Table 2, and a central reference view for each volume TF combination in Figure 9. The results show that the depth heuristic used and the image warping applied using this generalise well. The AngularEDSR network fails to generalise to unseen volumes and transfer functions. This is hardly surprisingly since the network has only ever seen one volume and transfer function. As such, the CNN currently has to be retrained for new volumes or TFs, but in future experiments we could attempt to generalise this learning.

Table 2: Average results on transfer function and volume combinations that are different from training.

	Warping		CNN	
TF, volume	PSNR	SSIM	PSNR	SSIM
New TF, head	36.50	0.956	34.46	0.955
Seen TF, head	41.43	0.949	40.18	0.949
New TF, heart	37.78	0.932	36.89	0.927

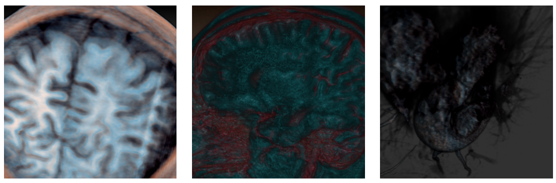

(a) New volume New TF (b) New volume Training TF (c) Seen volume New TF

Figure 9: Sample reference views used for synthesis of light fields on unseen data.

6 CONCLUSIONS AND FUTURE WORK

Applying depth heuristics for the purposes of image warping to synthesise views in light field volume rendering produces good results and we recommend this as a first step for this problem. Additionally, learning a residual light field improves the visual consistency of the geometrically based warping function, and is useful for views far away from the reference view. Our light field synthesis is fast compared to existing methods but is still too slow to compete with direct volume rendering in many cases. However, in contrast to light field volume rendering, the time for our synthesis is independent of the volume resolution and rendering effects and only depends on the resolution of the sample volume rendered image.

Our view synthesis results for light field volume rendering are of high quality and deep learning can be effectively be applied to this problem, but the geometrical image warping bottleneck prevents synthesis at interactive rates.

In future work, we would be keen to consider more datasets and transfer functions with various levels of transparency to help generalise this approach. We would also be interested in investigating further image warping procedures to identify potential optimisations. A possible technique for effective synthesis may be to use multiple depth heuristics and a CNN to combine them into one depth map. Moreover, incorporating additional volume information alongside a depth map and a volume rendered view could be beneficial. Given the expense of 3D CNNs learning over volumes, we expect that 2D CNNs learning from multiple images are likely to dominate in future years on volumetric data.

ACKNOWLEDGEMENTS

This research has been conducted with the financial support of Science Foundation Ireland (SFI) under Grant Number 13/IA/1895.

REFERENCES

Frayne, S. (2018). The looking glass. `https://lookingglassfactory.com/`. Accessed: 22/11/2018.

He, K., Zhang, X., Ren, S., and Sun, J. (2016). Deep residual learning for image recognition. In *Proceedings of the IEEE conference on computer vision and pattern recognition*, pages 770–778.

Kalantari, N. K., Wang, T.-C., and Ramamoorthi, R. (2016). Learning-based view synthesis for light field cameras. *ACM Transactions on Graphics*, 35(6):193:1–193:10.

Krizhevsky, A., Sutskever, I., and Hinton, G. E. (2012). Imagenet classification with deep convolutional neural networks. In *Advances in neural information processing systems*, pages 1097–1105.

Lanman, D. and Luebke, D. (2013). Near-eye light field displays. *ACM Transactions on Graphics (TOG)*, 32(6):220.

Levoy, M. and Hanrahan, P. (1996). Light Field Rendering. In *Proceedings of the 23rd annual conference on Computer graphics and interactive techniques*, SIGGRAPH '96, pages 31–42. ACM.

Lim, B., Son, S., Kim, H., Nah, S., and Lee, K. M. (2017). Enhanced deep residual networks for single image super-resolution. In *The IEEE conference on computer vision and pattern recognition (CVPR) workshops*, volume 1, page 4.

Lochmann, G., Reinert, B., Buchacher, A., and Ritschel, T. (2016). Real-time Novel-view Synthesis for Volume Rendering Using a Piecewise-analytic Representation. In *Vision, Modeling and Visualization*. The Eurographics Association.

Loshchilov, I. and Hutter, F. (2017). SGDR: Stochastic gradient descent with warm restarts. In *International Conference on Learning Representations*.

Mark, W. R., McMillan, L., and Bishop, G. (1997). Post-rendering 3d warping. In *Proceedings of the 1997 symposium on Interactive 3D graphics*, pages 7–16. ACM.

Mueller, K., Shareef, N., Huang, J., and Crawfis, R. (1999). Ibr-assisted volume rendering. In *Proceedings of IEEE Visualization*, volume 99, pages 5–8. Citeseer.

Paszke, A., Gross, S., Chintala, S., Chanan, G., Yang, E., DeVito, Z., Lin, Z., Desmaison, A., Antiga, L., and Lerer, A. (2017). Automatic differentiation in pytorch.

Penner, E. and Zhang, L. (2017). Soft 3d reconstruction for view synthesis. *ACM Transactions on Graphics*, 36(6):235:1–235:11.

Qi, C. R., Su, H., Nießner, M., Dai, A., Yan, M., and Guibas, L. J. (2016). Volumetric and multi-view cnns for object classification on 3d data. In *Proceedings of the IEEE conference on computer vision and pattern recognition*, pages 5648–5656.

Roettger, S. (2018a). Head volume dataset. `http://schorsch.efi.fh-nuernberg.de/data/volume/MRI-Head.pvm.sav`. Accessed: 24/08/2018.

Roettger, S. (2018b). Heart volume dataset. `http://schorsch.efi.fh-nuernberg.de/`

data/volume/Subclavia.pvm.sav. Accessed: 15/08/2018.

Shi, L., Hassanieh, H., Davis, A., Katabi, D., and Durand, F. (2014). Light field reconstruction using sparsity in the continuous fourier domain. *ACM Transactions on Graphics*, 34(1):1–13.

Simonyan, K. and Zisserman, A. (2014). Very deep convolutional networks for large-scale image recognition. *arXiv preprint arXiv:1409.1556*.

Srinivasan, P. P., Wang, T., Sreelal, A., Ramamoorthi, R., and Ng, R. (2017). Learning to sythesize a 4d rgbd light field from a single image. In *IEEE International Conference on Computer Vision (ICCV)*, pages 2262–2270.

Sundén, E., Steneteg, P., Kottravel, S., Jonsson, D., Englund, R., Falk, M., and Ropinski, T. (2015). Inviwo - an extensible, multi-purpose visualization framework. In *IEEE Scientific Visualization Conference (SciVis)*, pages 163–164.

Vagharshakyan, S., Bregovic, R., and Gotchev, A. (2018). Light field reconstruction using shearlet transform. *IEEE Transactions on Pattern Analysis and Machine Intelligence*, 40(1):133–147.

Wang, T.-C., Zhu, J.-Y., Hiroaki, E., Chandraker, M., Efros, A. A., and Ramamoorthi, R. (2016). A 4d light-field dataset and cnn architectures for material recognition. In *European Conference on Computer Vision*, pages 121–138. Springer.

Wanner, S. and Goldluecke, B. (2014). Variational light field analysis for disparity estimation and super-resolution. *IEEE Transactions on Pattern Analysis and Machine Intelligence*, 36(3):606–619.

Wanner, S., Meister, S., and Goldluecke, B. (2013). Datasets and benchmarks for densely sampled 4d light fields. In *Vision, Modeling, and Visualization*.

Wu, G., Zhao, M., Wang, L., Dai, Q., Chai, T., and Liu, Y. (2017). Light field reconstruction using deep convolutional network on epi. In *IEEE Conference on Computer Vision and Pattern Recognition (CVPR)*, pages 1638–1646.

Yoon, Y., Jeon, H.-G., Yoo, D., Lee, J.-Y., and So Kweon, I. (2015). Learning a deep convolutional network for light-field image super-resolution. In *Proceedings of the IEEE International Conference on Computer Vision Workshops*, pages 24–32.

Zellmann, S., Aumüller, M., and Lang, U. (2012). Image-based remote real-time volume rendering: Decoupling rendering from view point updates. In *ASME 2012 International Design Engineering Technical Conferences and Computers and Information in Engineering Conference*, pages 1385–1394. ASME.

Zhang, R., Isola, P., Efros, A. A., Shechtman, E., and Wang, O. (2018). The unreasonable effectiveness of deep features as a perceptual metric. In *Proceedings of the IEEE Conference on Computer Vision and Pattern Recognition (CVPR)*.